

Green peas in the southern sky: Broad-band color selection and spectroscopic follow up

YEJIN JEONG ¹, HYUNJIN SHIM ¹, EUNCHONG KIM ², AND JEONG HWAN LEE ^{3,4}

¹*Department of Earth Science Education, Kyungpook National University, 80 Daehak-ro, Daegu 41566, Republic of Korea*

²*International Gemini Observatory/NSF NOIRLab, 670 N. A'ohoku Place, Hilo, Hawaii, 96720, USA*

³*Research Institute of Basic Sciences, Seoul National University, Seoul 08826, Republic of Korea*

⁴*Department of Physics and Astronomy, Seoul National University, 1 Gwanak-ro, Gwanak-gu, Seoul 08826, Republic of Korea*

ABSTRACT

We present a systematic search for 1696 Green Pea (GP) galaxy candidates in the southern hemisphere selected from the Dark Energy Survey Data Release 2 (DES DR2) and provide preliminary results from spectroscopic follow-up observations of 26 targets chosen among them. Our selection criteria include the colors in *gri*-bands and compact morphology in the color composite images. The multi-wavelength spectral energy distribution fitting shows that the selected GP candidates exhibit star formation rates up to several tens $M_{\odot} \text{ yr}^{-1}$. With the mean stellar mass of $\log M_{*}/M_{\odot} = 8.6$, GP candidates are located at roughly 1 dex above the main sequence of star-forming galaxies at $z \sim 0.3$. Spectroscopic follow-up observations of the GP candidates with Gemini/GMOS are underway. All 26 targets are spectroscopically confirmed to be at $z = 0.3\text{--}0.41$ and have [OIII] equivalent width larger than 85 \AA , classified to be starbursts with low to moderate dust attenuation. These confirmed GPs show a lower metallicity offset from the mass-metallicity relation of local star-forming galaxies, indicating that GPs are less chemically evolved systems at their early stage of evolution.

Keywords: Galaxies (573) — Emission line galaxies (549) — Starburst galaxies (1570)

1. INTRODUCTION

Green Pea galaxies (hereafter GPs), which were first identified based on the green color and compact morphology in the SDSS *gri*-composite images (Cardamone et al. 2009), are characterized as starburst galaxies at $z \sim 0.3$ with strong [OIII] $\lambda 5007$ emission lines (corresponding to have large equivalent widths (EWs) up to $\sim 1000 \text{ \AA}$). Based on the physical properties of GPs studied so far – e.g., high star formation rate (SFR) for a given stellar mass (Cardamone et al. 2009; Brunner et al. 2020; Liu et al. 2022), low gas phase metallicity (Amorín et al. 2010, 2012; Izotov et al. 2011), and small size ($< 1 \text{ kpc}$; Yang et al. 2017a; Kim et al. 2020, 2021) –, GPs are considered to be low-redshift analogs of Ly α emitters at $z > 2$ with possibilities of Ly α photon escape (Henry et al. 2015; Yang et al. 2016). The leakage of the Lyman continuum is also observed in several GPs through the rest-frame UV observations (Izotov et al. 2016, 2018).

As the similarities between GPs and galaxies in the early Universe are claimed by the recent JWST observations of rest-frame spectra of $z \sim 8$ galaxies (Schaerer et al. 2022; Rhoads et al. 2023), GPs are getting attention as tools to probe the factors and processes related to the cosmic reionization.

GPs have inspired studies of ‘extreme emission line galaxies (EELGs)’ at different redshifts that have played important roles in galaxy evolution (de Barros et al. 2016; Li et al. 2018; Boyett et al. 2022). EELGs are characterized by high excitation nebular spectra with large EW emission lines. The observed line ratios in EELGs, such as high [OIII]/[OII], are often used as tracers of Ly α and Lyman continuum photon escape (Jaskot & Oey 2014; McKinney et al. 2019; Tang et al. 2019). EELG selection is also related to a search for extremely metal-poor galaxies (Bekki 2015), especially when there exist possibilities that different metallicity calibrators do not agree with each other in a low metallicity environment (Amorín et al. 2010; Curti et al. 2023).

Imaging surveys paralleled with the spectroscopic surveys in the northern sky (e.g., SDSS and LAMOST; York et al. 2000; Luo et al. 2015) have led to the con-

struction of the large GP sample in the northern hemisphere (e.g., Cardamone et al. 2009; Liu et al. 2022). However, there have been rare GP samples explored by the southern sky surveys including the Dark Energy Survey (DES; Abbott et al. 2021), which can be effective for a systematic search for GP candidates. It is also expected that the upcoming imaging and spectroscopic surveys such as the Legacy Survey of Space and Time (LSST; Ivezić et al. 2019) can contribute to constructing large samples of EELGs (including GPs) in the southern sky. Another advantage of exploring GPs in the southern sky area is the existence of surveys and instruments using multiple narrow- and medium-band filters, such as J-PLUS (Cenarro et al. 2019; Lumberras-Calle et al. 2022), J-PAS (Bonoli et al. 2021), and 7-Dimensional telescope (7DT; Im 2021), which would lead to more efficient selection of EELGs (e.g., Lumberras-Calle et al. 2022; Iglesias-Páramo et al. 2022). Comparison between the narrow- and medium-band filters information-aided selection and conventional broad-band color selection of strong line emitters would provide a hint to estimate sample completeness in these rare populations, complementing spectroscopic selection of EELGs.

In this study, we select GP candidates in the southern hemisphere based on the broad-band optical colors and morphology, in advance of the upcoming large and deep spectrophotometric surveys using narrow- and/or medium-band filters. The physical properties of the selected GP candidates and the scaling relations between those properties (SFR, stellar mass, and gas-phase metallicity) are explored through the broad-band spectral energy distribution (SED) fitting and follow-up spectroscopic observations.

The paper is organized as follows. In Section 2, we list our GP candidates selection process and the multi-wavelength photometry data of GP candidates compiled for the construction of the SED. In Section 3, we describe the SED fitting procedure (Section 3.1) and our spectroscopic follow-up observations made during the year 2024 (Section 3.2). Physical properties (photometric and spectroscopic redshifts, [OIII] line EWs, dust attenuation $E(B - V)$, SFR, stellar mass, and metallicity) and relations between them are presented in Section 4. Then we discuss the characteristics of the DES GPs through the comparison with the previously studied GP samples (constructed mostly in the northern hemisphere) along with our conclusion (Section 5). Throughout this paper, we use a flat cosmology model with the following parameters: $H_0 = 67.4 \text{ km s}^{-1} \text{ Mpc}^{-1}$, $\Omega_m = 0.315$, and $\Omega_\Lambda = 0.685$ (Planck Collaboration et al. 2020). All magnitudes are presented in the AB system.

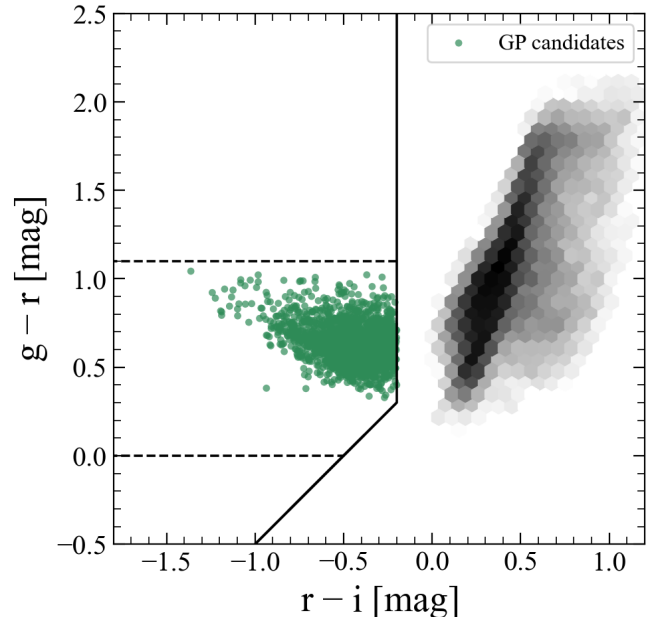


Figure 1. $(g-r)$ vs. $(r-i)$ color-color diagram constructed using DES photometry. Black hexagonal binned plots are randomly selected 0.1% of DES DR2 galaxies within the r -band magnitude range of $18.0 \leq r \leq 22.5$ (same as GPs), while green circles indicate GP candidates. Black solid lines indicate color selection criteria for GPs from Cardamone et al. (2009). Black dashed lines are the additional color cut we applied in this work, to avoid red galaxies.

2. SAMPLE

2.1. Green pea candidates selection

We selected candidates of the GPs from the second data release of the Dark Energy Survey (DES DR2; Abbott et al. 2021) covering $\sim 5,000 \text{ deg}^2$, based on their green colors and compact morphology in the optical images. When extracting photometric objects through the SQL query from the DESaccess¹, we applied constraints for the object flags (`flags_[grizY] < 2` and `imaflags_iso_[grizY] = 0`) to exclude objects that are affected by nearby bright stars. We also used the morphology constraint to remove stellar objects (using `wavg_spread_model_[i-band]`; Sevilla-Noarbe et al. 2018).

The extraction was also limited to objects that are observed in all of the five bands of the DES (i.e., `nepoch_[grizY] > 0`), having Petrosian radius less than or equal to 2 arcsec, considering the compactness of the green pea galaxies (Kim et al. 2021). Then we applied the color selection criteria for GPs as follows (the same as presented in Cardamone et al. 2009, with the addi-

¹ <https://des.ncsa.illinois.edu/desaccess/>

tional constraint for $(g - r)$ to avoid red galaxies):

$$\begin{aligned} r - i &\leq -0.2, \\ r - z &\leq 0.5, \\ g - r &\geq r - i + 0.5, \\ 0 &\leq g - r \leq 1.1. \end{aligned} \quad (1)$$

For magnitudes in Equation 1, we used `MAG_AUTO` from the `SExtractor` (`mag_auto_[grizY]`). While the SDSS and DES surveys utilize similar filter sets ($g, r, i,$ and z -bands), the actual filter responses are slightly different between the two surveys, causing magnitude offsets between the SDSS and DES bands. Therefore, to use the criteria of Cardamone et al. (2009), we applied a photometric transformation to the DES magnitudes using the formula from Abbott et al. (2021) to convert the magnitudes into SDSS magnitudes. In the case of the GP candidates, the magnitude offsets (i.e., $|g_{\text{SDSS}} - g_{\text{DES}}|$) were mostly smaller than 0.05 mag. In the magnitude range of $18.0 \leq r \leq 22.5$, the number of GP candidates satisfying the above color selection criteria was 6454. Figure 1 describes color selection criteria for GPs in the $(g - r)$ vs. $(r - i)$ color-color diagram.

Then we performed a visual inspection of the gri color-composite images of the color-selected GP candidates to exclude image artifacts (such as satellite trails), objects that are not as compact as pea-like galaxies, and objects with reddish colors. Stars were removed from the GP candidates by searching for matches to Gaia Data Release 3 parallax and proper motion measurements (Gaia Collaboration et al. 2023). The number of GP candidates after the visual inspection and star removal is 1696. These 1696 GP candidates comprise our DES GP (candidates) sample studied in this work.

Figure 2 shows the i -band magnitude distribution of the DES GP candidates (before and after the visual inspection) compared to that of the SDSS GPs from the early data release (DR7; Cardamone et al. 2009). The magnitude distributions before and after the visual inspection are consistent with each other in all optical bands ($g, r, i,$ and z -band), implying that the visual inspection does not result in a sample selection biased to the bright objects. The DES GP candidates we selected are fainter than the SDSS GPs, which is natural considering the high fraction of spectroscopically observed sources among the SDSS GPs. The mean i -band magnitudes of the DES and SDSS GPs are 21.75 and 20.20 mag, respectively. The ~ 1.5 mag difference on average suggests that GP candidates selected in the DES are fainter (and thus less massive) versions of the conventional SDSS GPs.

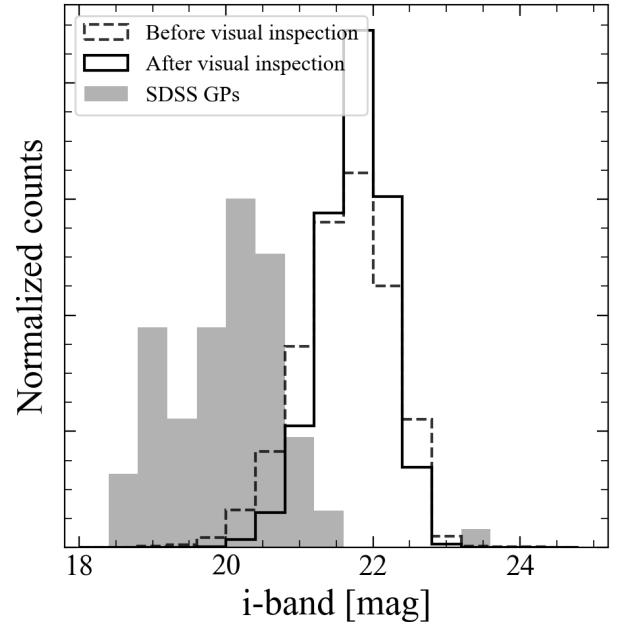


Figure 2. The i -band magnitude distributions of our DES GP candidates (selected in this study) and 80 SDSS GPs (Cardamone et al. 2009). The dashed and solid line represent the magnitude distributions before and after the visual inspection, respectively. Gray-filled histogram shows the SDSS GPs. Note that the total area under the histogram equals 1 in all cases.

2.2. Multi-wavelength photometry

To construct SEDs of the GP candidates, we compiled multi-wavelength photometry data from the ultraviolet (UV) to near-infrared (NIR) wavelengths. UV magnitudes of the DES GP candidates were extracted from the source catalog of the GALEX All-sky Imaging Survey Data Release 6 (Bianchi et al. 2014) using a matching radius of 3 arcsec. The total number of the matched sources is 1176, while the number of sources with available fluxes at both FUV (1500 Å) and NUV (2300 Å) bands is 604.

To compare the UV photometric properties of the DES GPs with those of other galaxies, we selected 50000 non-GP galaxies from the DES with the same i -band magnitude distribution as the GP candidates, of which 467 galaxies have flux measurements in both FUV and NUV bands. Figure 3 compares color-magnitude diagrams of the GP candidates and magnitude-matching non-GPs in the UV and optical wavelengths. GP candidates are slightly brighter in the UV wavelengths (median magnitudes of 21.53 and 22.04 mag in FUV and NUV bands) than non-GPs (median magnitudes of 23.18 and 22.64 mag in FUV and NUV bands, respectively). In addition, the $(\text{FUV} - \text{NUV})$ colors of the GP candidates are

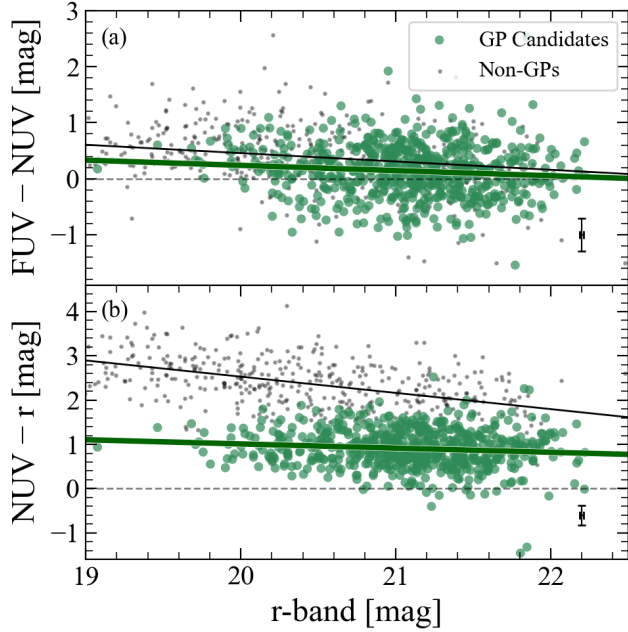


Figure 3. (a) $(FUV-NUV)$ color and (b) $(NUV-r)$ color vs. r -band magnitude diagram constructed using GALEX and DES photometry. Green circles and solid lines represent GPs and their trend lines, while black points and solid lines indicate Non-GPs and their trend lines, respectively. Error bars in the bottom right of each panel represent average errors in colors.

on average 0.3 mag bluer than those of the non-GPs at $r = 20$ mag, with little dependence on the r -band magnitudes for the color offset. The color difference is even more significant in the case of $(NUV-r)$ colors: non-GP galaxies exhibit the color-magnitude relation (i.e., brighter galaxies are redder), however, such a trend is relatively weak in the case of GP candidates. This implies that GP candidates are bluer galaxies compared to non-GP galaxies, because of being less dust-attenuated and/or having younger stellar populations.

NIR magnitudes of the GP candidates in 1-4 μm were compiled to estimate stellar masses of them based on the multi-wavelength SED fitting. We used two catalogs: (1) the VISTA Hemisphere Survey (VHS) Data Release 6 (McMahon et al. 2021) for photometry in J, H, and K-bands, and (2) the CatWISE2020 catalog (Marocco et al. 2021) for photometry in W1 (3.4 μm) and W2 (4.6 μm) bands. Using the matching radius of 1 arcsec, the number of the identified GP candidates in the VHS DR6 is 471, while most of them (468) are detected only in the J-band. We used a larger matching radius (2 arcsec) to find counterparts in the CatWISE2020 catalog since the WISE spatial resolution is relatively poor. In the CatWISE2020 catalog, we found matches for 389 GP candidates.

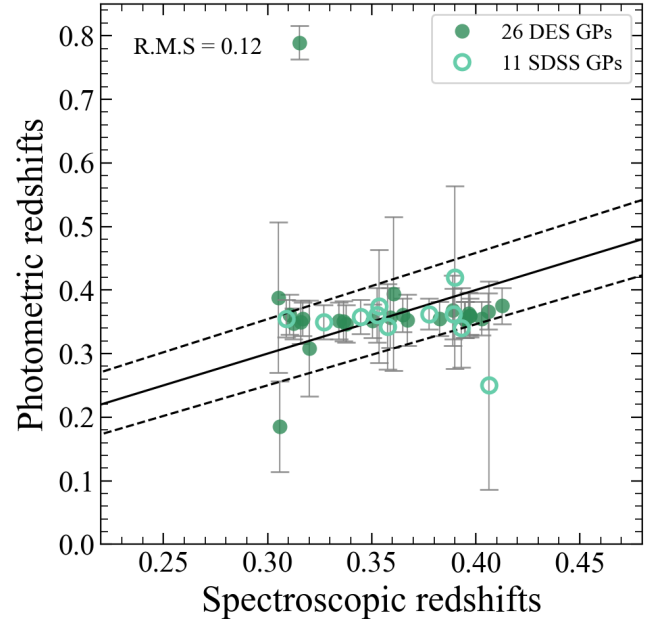


Figure 4. Comparison between spectroscopic redshifts and photometric redshifts derived from CIGALE SED fitting. The solid line shows the $y = x$ equation and the dashed lines show $|\Delta z|/(1+z) < 0.04$. Most of the spectroscopically observed GPs show $|\Delta z|/(1+z) < 0.04$, except for four cases including those with $z_{\text{phot}} < 0.26$ or $z_{\text{phot}} > 0.4$.

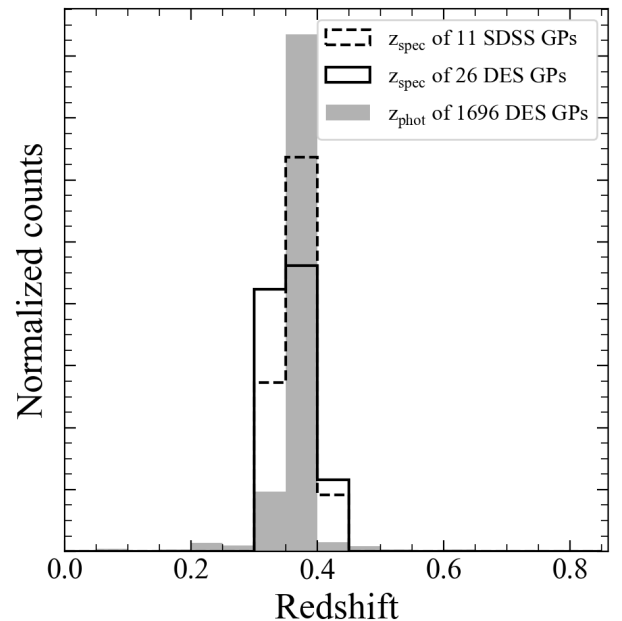


Figure 5. Redshift distributions of SDSS and DES GPs (for both spectroscopic and photometric redshift). Note that the histograms are normalized so that the total area under the histogram is equal to 1.

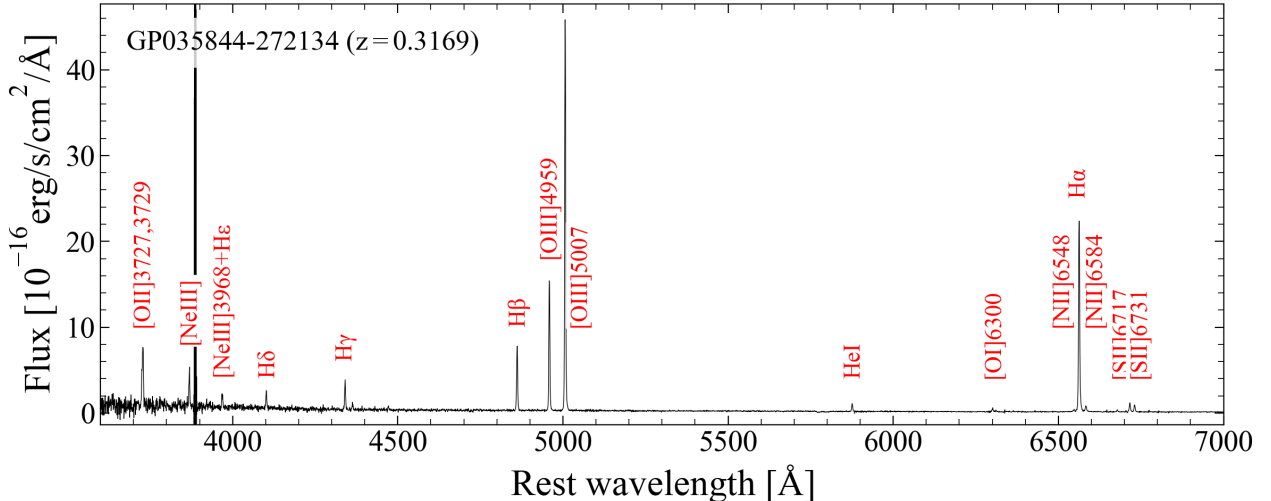


Figure 6. The spectrum of the GP035844-272134, which has the strongest line fluxes among 26 GPs in our Gemini GMOS-S spectroscopic follow-up program, is presented as an example in the rest-frame wavelength range of 3600-7000 Å.

3. METHODS

3.1. Multi-wavelength SED fitting

We estimated the physical properties of the GP candidates, including SFR, stellar mass, $E(B-V)$, and equivalent width (EW) of the [OIII] emission line, through the multi-wavelength SED fitting with the use of CIGALE (Boquien et al. 2019). We used all of the compiled photometric data points that are available, i.e., magnitudes in the FUV, NUV, g , r , i , z , Y , J , H , K , $W1$, and $W2$ -bands. The number of GP candidates with magnitudes in more than 6 out of the 12 photometric bands is 1318, while 412 GP candidates have fluxes in more than 8 photometric bands.

To determine the most appropriate parameters and configurations for the SED fitting, we used 11 objects among our 1696 GP candidates that have been spectroscopically observed in SDSS DR18. These 11 GPs have spectroscopic redshifts of $z = 0.35-0.42$, with strong [OIII] emission lines present in their spectra. By changing the modules and parameter values (ranges and steps) in each module, we tried to reproduce the spectroscopic redshifts and [OIII] $\lambda 5007$ EWs of these objects using the photometric redshift mode of the CIGALE. In the photometric redshift mode, the photometric redshifts were obtained using a Bayesian analysis based on the SED fitting, searching for the best-fitting redshift in the range of $z = 0.05$ to 1.0 at intervals of 0.01.

The finally selected modules and parameter value settings are summarized in Table 1. We used a delayed star formation history (`sfhdelayed`), `bc03` stellar population synthesis model (Bruzual & Charlot 2003), Chabrier initial mass function (Chabrier 2003), nebular emission and dust attenuation. Although we used modules for AGN

emission (fritz2006) and dust emission (d12014), we fixed the AGN luminosity fraction to be zero and did not use a range of parameters in the dust emission module, because the AGN and dust emission modules can only be constrained by the photometry at wavelengths longer than the mid-infrared. In the nebular emission module, we used a wide range of ionization parameter U , gas metallicity, and line width to reproduce the spectroscopic EW. With these settings, we could derive photometric redshifts with the accuracy of $|\Delta z|/(1+z) < 0.04$ at $0.3 < z < 0.45$ (Figures 4 and 5), which were confirmed later with the additional 26 spectroscopic redshifts obtained from our observations (Section 3.2).

3.2. Follow-up spectroscopic observation

To test the efficiency of sampling strong [OIII] emitters in the DES region based on the GP color selection technique, we initiated the spectroscopic follow-up observation program for GP candidates with the Gemini Multi-Object Spectrograph (GMOS) on Gemini-South, utilizing long-slit observing mode at relatively poor weather conditions (Bands 3 and 4). While the observation program is still an ongoing project, the spectra of 26 GP candidates that have been obtained over the period of April to September 2024 are presented in this paper. We used R400 grating with two central wavelength settings (7000Å and 7500Å) to avoid the line falling in the gaps between the CCD chips. Our spectrum covers the wavelength range of 3600-10300 Å. With a 0.5 arcsec width slit and no binning in spectral direction, the spectral dispersion was 0.85Å pixel^{-1} resulting in $R \sim 1800$. The on-source integration time was either 2400 seconds ($600 \text{s} \times 4$, consisting of four ABBA dithering for sky background removal) or 3000 seconds ($750 \text{s} \times 4$), which

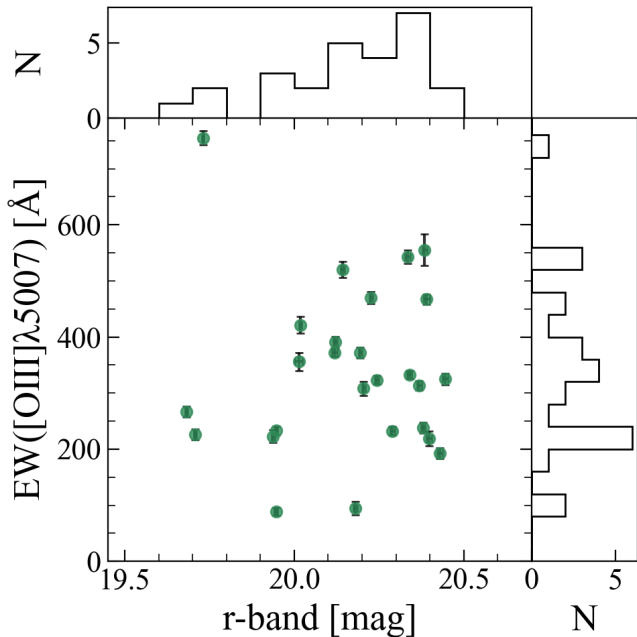


Figure 7. $[\text{OIII}]\lambda 5007$ equivalent width vs. r -band magnitude for 26 GPs that are spectroscopically observed.

was determined based on the r -band magnitude of the target.

The spectra were reduced in a standard manner (i.e., bias/flat correction, wavelength calibration, distortion correction, and 1-D spectra extraction) using the DRAGONS² (Data Reduction for Astronomy from Gemini Observatory North and South; Labrie et al. 2023). The baseline calibration (using spectrophotometric standard star observation) and the aperture extraction were done in an interactive mode, with caution paid to prevent overfitting in sensitivity function calculation and aperture tracing.

Figure 6 shows an example of the reduced GP spectrum obtained through our program. Similarly to the previously confirmed GPs (e.g., Cardamone et al. 2009), the spectrum shows numerous nebular emission lines, including strong $[\text{OIII}]$ and Hydrogen Balmer lines. The coordinates, r -band magnitudes, spectroscopic redshifts along with the stellar mass and SFR estimated from the multi-wavelength SED fitting (Section 3.1) are summarized in Table 2. Spectroscopic redshifts of the observed objects range $z = 0.3\text{--}0.41$. It is not straightforward to calculate the completeness or the purity of our GP selection strategy with limited numbers of spectroscopically followed targets. However, the fact that all targets lie at $z \sim 0.3$ and show strong $[\text{OIII}]$ indicates that our

selection is effective to search for GPs at $z \sim 0.3$ and is relatively free from contaminations of emission-line galaxies at other redshifts.

4. RESULTS

4.1. Redshift distribution

As is discussed in Section 3.1, the photometric redshift accuracy of our SED fitting is $|\Delta z|/(1+z) < 0.04$. In addition to the comparison between spectroscopic and photometric redshifts (Figure 4), Figure 5 shows the photometric redshift distribution of the 1696 GP candidates as well as spectroscopic redshift distribution of the spectroscopically observed GPs. Although the spectroscopic target selection is inevitably biased to the bright targets, the redshift distributions of the spectroscopic subsample and the parent photometric sample are consistent with each other. The mean value of the photometric redshift is $\langle z \rangle = 0.36$, with a standard deviation of 0.05.

The photometric redshift range of GP candidates selected in the DES is slightly higher than that of GPs selected in the SDSS ($0.112 \leq z \leq 0.360$, Cardamone et al. 2009). The difference appears to reflect the difference in filter systems. The central wavelengths of the DES gri filters are slightly longer (4808, 6417, and 7814 Å) than that of the SDSS gri filters (4702, 6175, and 7489 Å). The green color of the GPs in the gri color-composite images require strong $[\text{OIII}]$ emission line that is redshifted into the r -band wavelength range, which naturally explains GPs selected in the DES images having slightly higher redshifts.

4.2. $[\text{OIII}]\lambda 5007$ EWs

For 26 GP targets of the GMOS follow-up spectroscopic observations, we measured line flux and EW of noticeable emission lines (with the line $S/N > 3$) using the JDAVIZ/SPECVIZ tool (Developers et al. 2024) in the interactive mode (Tables 3 and 4). As it is expected from the green color in the gri images, GPs are considered to have strong $[\text{OIII}]$ emission lines, with EW ranging up to a few hundreds Å (Table 4). Figure 7 shows the distribution of the $[\text{OIII}]\lambda 5007$ EW as a function of the r -band magnitude, which does not show any correlation between the two. This implies that (although the number of galaxies used here is small) the r -band magnitude cut for strong line emitter selection would not place bias in sample selection in terms of the line EW. This is consistent with the previous studies suggesting that the fractions of the EELGs do not vary significantly with UV luminosity among UV-selected star-forming galaxies (Boyet et al. 2022), considering that large EW corresponds to high ongoing SFR.

² <https://zenodo.org/records/10841622>

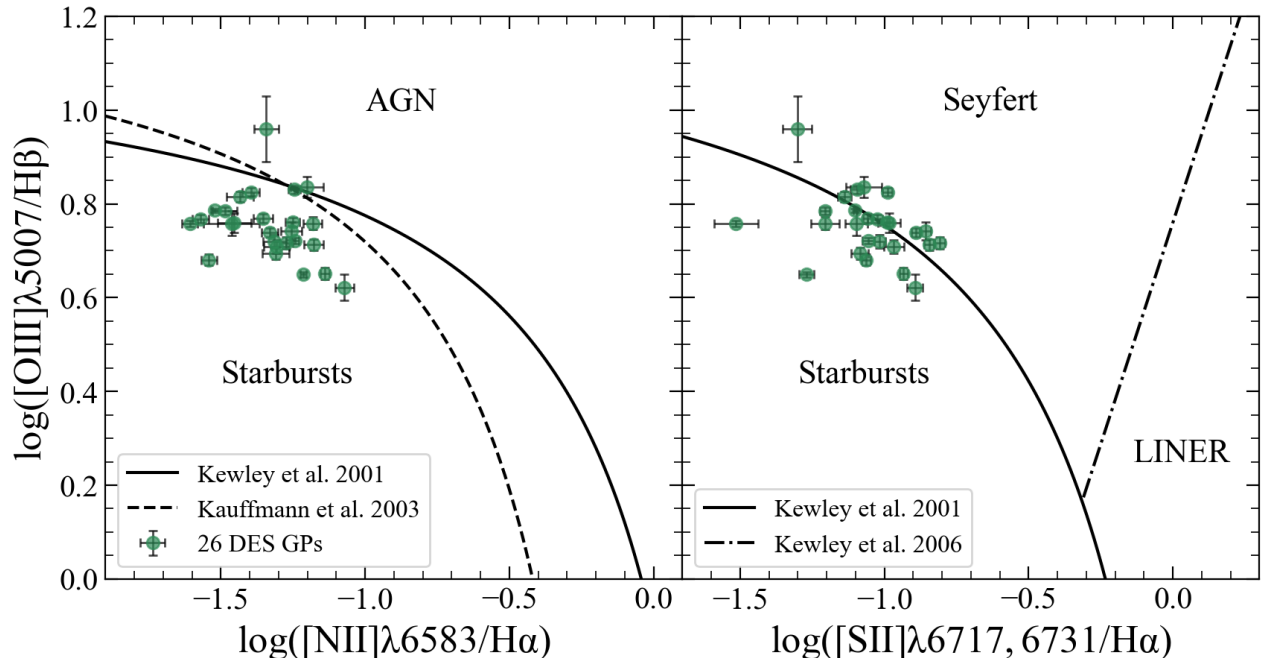


Figure 8. BPT diagrams (Baldwin et al. 1981) to classify galaxies into starbursts and AGN (left), as well as into starbursts, Seyferts, and LINER (right). Solid and dashed lines are dividers for starbursts and AGN from Kewley et al. (2001) and Kauffmann et al. (2003), respectively. Dash-dot line is a suggested criterion to differentiate between Seyfert and LINER (Kewley et al. 2006).

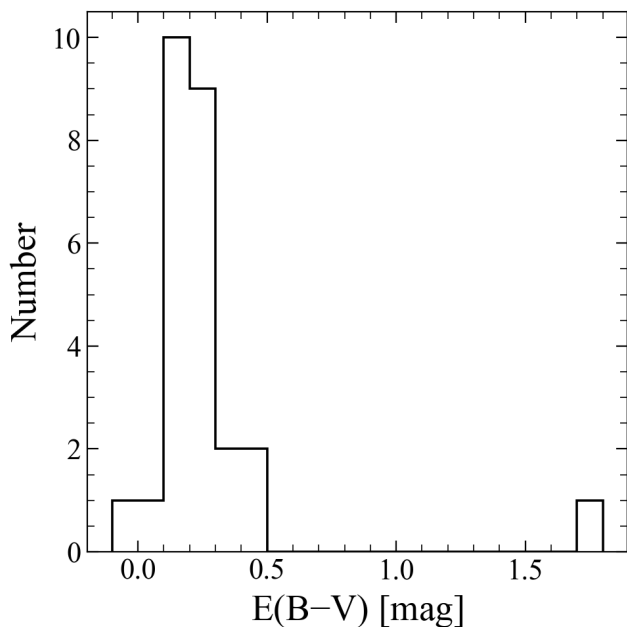


Figure 9. Color excess $E(B-V)_{\text{gas}}$ of the spectroscopically observed 26 GPs derived from the observed Balmer line ratios ($H\alpha/H\beta$). The Calzetti et al. (2000) dust attenuation curve was used.

The mean value of the observed $[OIII]\lambda 5007$ EW is 340\AA . Although there are numerous different criteria

for EW to define line emitters at different redshifts (e.g., Amorín et al. 2015; Tran et al. 2020; Iglesias-Páramo et al. 2022; Boyett et al. 2024), the mean value of the observed $[OIII]\lambda 5007$ EW, 340\AA , for DES spectroscopically observed GPs, is comparable to that of most strong line emitters.

4.3. AGN contamination

Figure 8 shows the BPT diagrams (Baldwin et al. 1981) to classify the spectral types of GPs into either starburst-dominated or AGN-dominated systems. Most (23 out of 26) GP candidates are classified as starbursts while only two objects (GP211619-463914, GP232739-454554) are classified as AGN and one object (GP204359-540359) is lying on the boundary. Despite most GPs being classified as starbursts, the possibility of them being close to Seyferts cannot be ruled out (right panel of Figure 8). However, the possible Seyfert-like objects do not show broad hydrogen recombination lines in the reduced spectra.

4.4. Dust attenuation

We used the Balmer decrement (observed line flux ratios between $H\alpha$ and $H\beta$; Table 3) to estimate dust attenuation of the GPs. Considering that our GPs are mostly star-forming galaxies (Figure 8), we used the extinction curve for starburst galaxies (Calzetti et al.

2000). The color excess $E(B - V)$ was calculated using the following formula:

$$E(B - V)_{\text{gas}} = \frac{2.5 \times \log_{10}[(f_{\text{H}\alpha}/f_{\text{H}\beta})/2.86]}{k(\text{H}\beta) - k(\text{H}\alpha)}, \quad (2)$$

where the $k(\text{H}\alpha)$ and $k(\text{H}\beta)$ values were taken from Calzetti (2001), and the intrinsic $(f_{\text{H}\alpha}/f_{\text{H}\beta})$ was considered to be 2.86 assuming the case B recombination with $T = 10^4$ K and $n_e = 10^4$ cm $^{-3}$. Figure 9 shows the $E(B - V)_{\text{gas}}$ distribution of the spectroscopically observed GPs. The median value is $E(B - V)_{\text{gas}} = 0.21$, while most GPs showing color excess less than 0.5 mag except one object (GP232739-454554) with very low H β line flux. The spectrum of the GP232739-454554 shows lower S/N in the shorter wavelength than in the longer wavelength. Therefore, the fact that the S/N of the H β line being low is thought to be the reason of high attenuation in this object. Similarly to previous studies on the attenuation in GPs (e.g., Cardamone et al. 2009; Liu et al. 2022), our GPs are relatively blue galaxies (which is consistent with their UV to optical colors in Figure 3) with little dust attenuation.

4.5. SFR vs. stellar mass

The distributions of stellar mass and SFR of the GP candidates are presented in Figure 10. The stellar mass of the most GP candidates ranges 10^8 - 10^9 M_{\odot} , with a mean value of $\langle M_{\text{star}} \rangle = 10^{8.6}$ M_{\odot} . This places the DES GP candidates in the lowest regime of the stellar mass ($10^{8.5}$ - 10^{10} M_{\odot}) among the early SDSS GPs (Cardamone et al. 2009), which is natural considering that DES GPs are ~ 1.5 mag fainter than that of the SDSS GPs (Figure 2).

GP candidates exhibit SFR ranging a few to several tens $M_{\odot} \text{ yr}^{-1}$, therefore the typical specific SFR (sSFR) value, i.e., SFR divided by the stellar mass, is $\sim 10^{-8} \text{ yr}^{-1}$. Compared to the main sequence of star-forming galaxies at $z = 0.3$ - 0.41 (Speagle et al. 2014), GP candidates show an order of magnitude higher SFR at the same stellar mass. The sSFR of the GP candidates are comparable to that of $z = 6$ star-forming main sequence galaxies, indicating that the GP selection may lead to a selection of local analogs of high-redshift star-forming galaxies that are responsible for cosmic reionization.

4.6. Mass-metallicity relation

For 26 spectroscopically observed GPs, we estimated the gas-phase metallicity $12 + \log(\text{O}/\text{H})$ based on the empirical $N2$ ($\equiv \log([\text{NII}]\lambda 6584/\text{H}\alpha)$) method (Pettini & Pagel 2004) that uses strong emission lines:

$$12 + \log(\text{O}/\text{H}) = 8.90 + (0.57 \times N2). \quad (3)$$

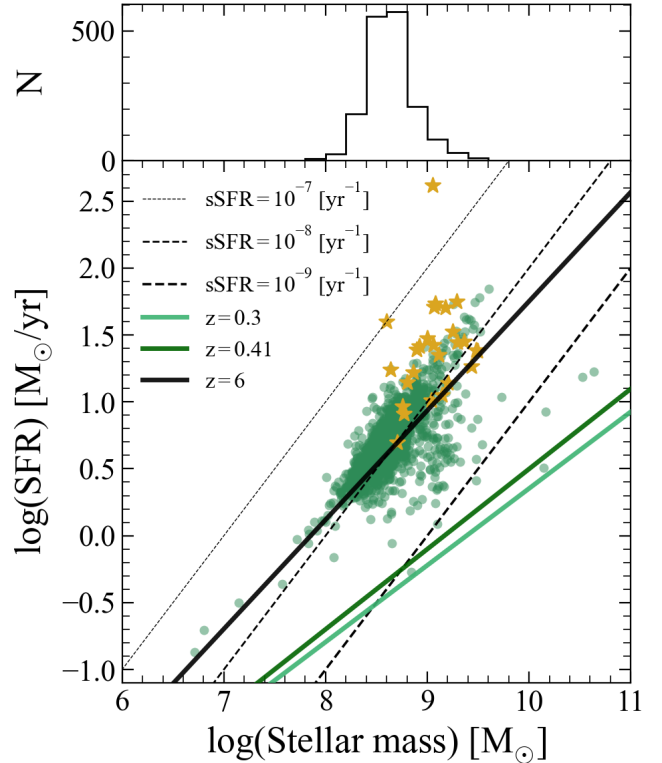


Figure 10. The SFR vs. stellar mass for the 1696 GPs estimated by CIGALE with the distribution of stellar mass. The dashed lines represent specific star formation rates (sSFR) of 10^{-7} , 10^{-8} and 10^{-9} yr^{-1} , respectively. Most of the GPs are located along the sSFR line of 10^{-8} yr^{-1} , with a few GPs positioned along 10^{-9} yr^{-1} line. Solid lines represent the star-forming main sequence (SFMS) relations with $z = 0.3$, 0.41 and 6 using the redshift evolution of star-forming main sequence suggested by Speagle et al. (2014). Filled stars represent 26 spectroscopically observed GPs, for which SFR is calculated based on the extinction-corrected H α line flux.

The values are listed in Table 2 along with the stellar masses and SFR estimated from the SED fitting. GPs have oxygen abundances $12 + \log(\text{O}/\text{H}) < 8.3$, with the mean value of $\langle 12 + \log(\text{O}/\text{H}) \rangle = 8.14$ (i.e., $\sim 30\%$ the solar value; Allende Prieto et al. 2001). In the mass-metallicity diagram (Figure 11), GPs lie under the 95% confidence interval of the local star-forming galaxies (Tremonti et al. 2004). At the same time, GPs follow a similar mass-metallicity trend at low metallicities that more massive systems follow at higher metallicities. Such a trend, as well as gas phase metallicity range, is consistent with the previous studies on the [OIII]-selected GPs (e.g., Brunner et al. 2020). This supports the idea that GP selection is an efficient strategy to sample low metallicity galaxies, as the strong line emitters tend to be chemically less evolved systems undergoing their early stage of star formation.

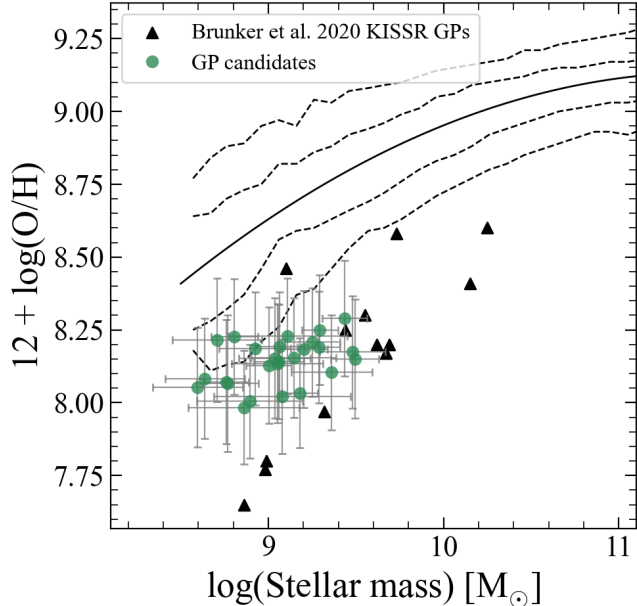


Figure 11. Gas-phase metallicity ($12 + \log(\text{O}/\text{H})$) vs. stellar mass of 26 GPs (green circles). Overplotted solid line is the mass-metallicity relation of star-forming galaxies at $z \sim 0.1$, while the dashed lines represent 68% and 95% of the mass-metallicity distribution (Tremonti et al. 2004). Filled triangles are GPs from the KPNO International Spectroscopic Survey (Brunker et al. 2020).

5. DISCUSSION & CONCLUSION

We selected GP candidates from the DES DR2 that covers $\sim 5,000 \text{ deg}^2$ of the southern sky, and investigated their properties using the multi-wavelength SED fitting. In total, 1696 GP candidates were selected by applying broad-band color criteria (Cardamone et al. 2009) and through visual inspection on the *gri* color composite images. Using the multi-wavelength photometry covering from UV to NIR, GP candidates were found to be low-mass ($10^{6.71}-10^{10.63} M_{\odot}$), highly star-forming ($\log(\text{SFR}) = -0.87-1.85$) galaxies at the mean photometric redshift of $\langle z_{\text{phot}} \rangle = 0.36$. Early results from our spectroscopic follow-up program for DES GPs suggest that all 26 GP targets do show strong [OIII] emission lines with EW larger than $\sim 85 \text{ \AA}$, related to a low metallicity (less than 30% the solar metallicity) and insignificant attenuation in these systems.

Since our GP candidates sample is one of the starting points to construct strong line emitters in the southern hemisphere where numbers of large imaging/spectroscopic surveys are planned, we list major characteristics of our GP candidates that are common with or different from the previously constructed GP samples (e.g., SDSS DR7, Cardamone et al. 2009; SDSS

DR13, Jiang et al. 2019; Harish et al. 2023; SDSS DR16, Ding et al. 2023; KISS, Brunker et al. 2020; LAMOST DR9, Lumbreras-Calle et al. 2022).

1. DES GPs are expected to lie at slightly higher redshifts than SDSS GPs, since the central wavelengths of the DES *g*, *r*, and *i*-bands are longer than that of the corresponding SDSS bands.

2. DES GPs are on average less massive ($10^{8.6} M_{\odot}$) than SDSS GPs ($10^{9.5} M_{\odot}$), which is natural that DES GPs are $\sim 1.5 \text{ mag}$ fainter. While the DES GPs occupy the lowest mass regime among the GP population, the sSFR remains to be relatively consistent over the two orders of the stellar mass range.

3. [OIII] EWs of the spectroscopically observed DES GPs are comparable to that of SDSS GPs. The lack of the extremely large EW (reaching up to $\sim 1000 \text{ \AA}$) galaxies might be due to the small size of the targets. Similarly in the case of the SDSS GPs, little correlation exists between the *r*-band magnitudes and [OIII] EW.

4. Judging from the spectroscopically observed DES GPs, starburst-dominated systems dominate the GP population rather than AGN-dominated systems. The AGN fraction is uncertain (2-4 out of 26), however the value partly overlaps with that of the search for MIR AGN among SDSS GPs.

5. Spectroscopically observed DES GPs show mass-metallicity relation over ~ 1 order of stellar mass range that more massive GPs show higher gas-phase metallicity. This mass-metallicity relation is about 0.5 dex lower than from the mass-metallicity relation of local star-forming galaxies, and is consistent with the SDSS and KISSR GPs.

The spatial number density of the DES GPs is 0.34 deg^{-2} , considering the number of GPs is 1696 from the 5000 deg^2 covered in the DES DR2. This is smaller than that of the early SDSS GPs (about 2 deg^{-2} ; Cardamone et al. 2009) or emission line searches in the wider redshift range (e.g., $0.11 < z < 0.93$, $30-100 \text{ deg}^{-2}$; Amorín et al. 2015; Iglesias-Páramo et al. 2022), yet is comparable or larger than that of the local ($z < 0.06$) extreme line emitters (e.g., $0.0003-0.23 \text{ deg}^{-2}$ Yang et al. 2017b; Lumbreras-Calle et al. 2022). While it is difficult to quantify the sample completeness considering that broad-band magnitude limits as well as EW limits that can be probed by different surveys are different, the *r*, *i*, and *z*-band magnitude distributions of the DES GPs suggests that the number of the GPs in a specific magnitude bin increases as the magnitude gets fainter. Considering these, the number of GPs (as well as extreme line emitters) would increase through the deep imaging

surveys planned in the southern hemisphere (e.g., LSST; Ivezić et al. 2019) that also cover wide, unexplored area. Our DES GP sample, although photometrically selected yet expected to have high purity judged by the spectroscopic follow up, could be used as a reference data set to complement the future selection strategy for strong line emitters in the southern sky.

1 This work was supported by the National Research
2 Foundation of Korea (NRF) grant funded by the Ko-
3 rea government (MSIT) (Nos. 2022R1A4A3031306, RS-
4 2024-00349364). J.H.L. acknowledges support from Ba-
5 sic Science Research Program through the National Re-
6 search Foundation of Korea (NRF) funded by the Min-
7 istry of Education (No. RS-2024-00452816). This work
8 was supported by K-GMT Science Program (PID: GS-
9 2024A-Q-313, GS-2024A-Q-411, GS-2024B-Q-313) of
10 Korea Astronomy and Space Science Institute (KASI).
11 Section 3.2 and following results are based on obser-
12 vations obtained at the international Gemini Observa-
13 tory, a program of NSF NOIRLab, which is managed by
14 the Association of Universities for Research in Astron-
15 omy (AURA) under a cooperative agreement with the
16 U.S. National Science Foundation on behalf of the Gem-
17 ini Observatory partnership: the U.S. National Science
18 Foundation (United States), National Research Council
19 (Canada), Agencia Nacional de Investigación y Desar-
20 rollo (Chile), Ministerio de Ciencia, Tecnología e Inno-
21 vación (Argentina), Ministério da Ciência, Tecnologia,
22 Inovações e Comunicações (Brazil), and Korea Astron-
23 omy and Space Science Institute (Republic of Korea).

Facility: Gemini:South

Software: astropy (Astropy Collaboration et al. 2013, 2018), jdaviz (Developers et al. 2024)

REFERENCES

- Abbott, T. M. C., Adamów, M., Agüena, M., et al. 2021, ApJS, 255, 20, doi: [10.3847/1538-4365/ac00b3](https://doi.org/10.3847/1538-4365/ac00b3)
- Allende Prieto, C., Lambert, D. L., & Asplund, M. 2001, ApJL, 556, L63, doi: [10.1086/322874](https://doi.org/10.1086/322874)
- Amorín, R., Pérez-Montero, E., Vílchez, J. M., & Papaderos, P. 2012, ApJ, 749, 185, doi: [10.1088/0004-637X/749/2/185](https://doi.org/10.1088/0004-637X/749/2/185)
- Amorín, R., Pérez-Montero, E., Contini, T., et al. 2015, A&A, 578, A105, doi: [10.1051/0004-6361/201322786](https://doi.org/10.1051/0004-6361/201322786)
- Amorín, R. O., Pérez-Montero, E., & Vílchez, J. M. 2010, ApJL, 715, L128, doi: [10.1088/2041-8205/715/2/L128](https://doi.org/10.1088/2041-8205/715/2/L128)
- Astropy Collaboration, Robitaille, T. P., Tollerud, E. J., et al. 2013, A&A, 558, A33, doi: [10.1051/0004-6361/201322068](https://doi.org/10.1051/0004-6361/201322068)
- Astropy Collaboration, Price-Whelan, A. M., Sipőcz, B. M., et al. 2018, AJ, 156, 123, doi: [10.3847/1538-3881/aabc4f](https://doi.org/10.3847/1538-3881/aabc4f)
- Baldwin, J. A., Phillips, M. M., & Terlevich, R. 1981, PASP, 93, 5, doi: [10.1086/130766](https://doi.org/10.1086/130766)
- Bekki, K. 2015, MNRAS, 454, L41, doi: [10.1093/mnras/1slv117](https://doi.org/10.1093/mnras/1slv117)
- Bianchi, L., Conti, A., & Shiao, B. 2014, VizieR Online Data Catalog: GALEX-GR6/7 data release (Bianchi+2014), VizieR On-line Data Catalog: II/335. Originally published in: 2014AdSpR...53..900B
- Bonoli, S., Marín-Franch, A., Varela, J., et al. 2021, A&A, 653, A31, doi: [10.1051/0004-6361/202038841](https://doi.org/10.1051/0004-6361/202038841)
- Boquien, M., Burgarella, D., Roehly, Y., et al. 2019, A&A, 622, A103, doi: [10.1051/0004-6361/201834156](https://doi.org/10.1051/0004-6361/201834156)
- Boyett, K., Bunker, A. J., Curtis-Lake, E., et al. 2024, MNRAS, 535, 1796, doi: [10.1093/mnras/stae2430](https://doi.org/10.1093/mnras/stae2430)
- Boyett, K. N. K., Stark, D. P., Bunker, A. J., Tang, M., & Maseda, M. V. 2022, MNRAS, 513, 4451, doi: [10.1093/mnras/stac1109](https://doi.org/10.1093/mnras/stac1109)
- Brunker, S. W., Salzer, J. J., Janowiecki, S., Finn, R. A., & Helou, G. 2020, ApJ, 898, 68, doi: [10.3847/1538-4357/ab9ec0](https://doi.org/10.3847/1538-4357/ab9ec0)

Table 1. Parameters for CIGALE SED fitting

Modules and input parameters	Range
Star formation history: <code>sfhdelayed</code>	
e-folding time of the main stellar population model [Myr]	2000
Age of the main stellar population [Myr]	50, 100, 200, 500,700, 1000, 1500, 2000, 4000, 6000, 8000, 12000
e-folding time of the late starburst population model [Myr]	50
Age of the late burst [Myr]	20
Mass fraction of the late burst population	0.0, 0.15
Stellar population: <code>bc03</code>	
Initial mass function	Chabrier
Metallicity	0.004, 0.008, 0.02
Nebular emission: <code>nebular</code>	
Ionization parameter	-4.0, -3.0, -2.8, -2.6, -2.4, -2.2, -1.6, -1.2, -1.0
Gas metallicity	0.004, 0.008, 0.014, 0.019
Electron density	10, 100, 1000
Fraction of Lyman continuum photons escaping the galaxy	0.0
Fraction of Lyman continuum photons absorbed by dust	0.0
Line width [km/s]	25, 50, 75, 100
Include nebular emission	True
Dust attenuation: <code>dustatt.modified.starburst</code>	
E(B-V) lines	0.0, 0.05, 0.1, 0.2, 0.3, 0.4, 0.5

- Bruzual, G., & Charlot, S. 2003, MNRAS, 344, 1000, doi: [10.1046/j.1365-8711.2003.06897.x](https://doi.org/10.1046/j.1365-8711.2003.06897.x)
- Calzetti, D. 2001, PASP, 113, 1449, doi: [10.1086/324269](https://doi.org/10.1086/324269)
- Calzetti, D., Armus, L., Bohlin, R. C., et al. 2000, ApJ, 533, 682, doi: [10.1086/308692](https://doi.org/10.1086/308692)
- Cardamone, C., Schawinski, K., Sarzi, M., et al. 2009, MNRAS, 399, 1191, doi: [10.1111/j.1365-2966.2009.15383.x](https://doi.org/10.1111/j.1365-2966.2009.15383.x)
- Cenarro, A. J., Moles, M., Cristóbal-Hornillos, D., et al. 2019, A&A, 622, A176, doi: [10.1051/0004-6361/201833036](https://doi.org/10.1051/0004-6361/201833036)
- Chabrier, G. 2003, PASP, 115, 763, doi: [10.1086/376392](https://doi.org/10.1086/376392)
- Curti, M., D'Eugenio, F., Carniani, S., et al. 2023, MNRAS, 518, 425, doi: [10.1093/mnras/stac2737](https://doi.org/10.1093/mnras/stac2737)
- de Barros, S., Vanzella, E., Amorín, R., et al. 2016, A&A, 585, A51, doi: [10.1051/0004-6361/201527046](https://doi.org/10.1051/0004-6361/201527046)
- Developers, J., Averbukh, J., Bradley, L., et al. 2024, Jdaviz, v4.0.0, Zenodo, doi: [10.5281/zenodo.5513927](https://doi.org/10.5281/zenodo.5513927)
- Ding, W., Zou, H., Kong, X., et al. 2023, AJ, 166, 133, doi: [10.3847/1538-3881/ace893](https://doi.org/10.3847/1538-3881/ace893)
- Gaia Collaboration, Vallenari, A., Brown, A. G. A., et al. 2023, A&A, 674, A1, doi: [10.1051/0004-6361/202243940](https://doi.org/10.1051/0004-6361/202243940)
- Harish, S., Malhotra, S., Rhoads, J. E., et al. 2023, ApJ, 945, 157, doi: [10.3847/1538-4357/acb99c](https://doi.org/10.3847/1538-4357/acb99c)
- Henry, A., Scarlata, C., Martin, C. L., & Erb, D. 2015, ApJ, 809, 19, doi: [10.1088/0004-637X/809/1/19](https://doi.org/10.1088/0004-637X/809/1/19)
- Iglesias-Páramo, J., Arroyo, A., Kehrig, C., et al. 2022, A&A, 665, A95, doi: [10.1051/0004-6361/202243931](https://doi.org/10.1051/0004-6361/202243931)
- Im, M. 2021, in 43rd COSPAR Scientific Assembly. Held 28 January - 4 February, Vol. 43, 1537
- Ivezić, Ž., Kahn, S. M., Tyson, J. A., et al. 2019, ApJ, 873, 111, doi: [10.3847/1538-4357/ab042c](https://doi.org/10.3847/1538-4357/ab042c)
- Izotov, Y. I., Guseva, N. G., & Thuan, T. X. 2011, ApJ, 728, 161, doi: [10.1088/0004-637X/728/2/161](https://doi.org/10.1088/0004-637X/728/2/161)
- Izotov, Y. I., Schaerer, D., Thuan, T. X., et al. 2016, MNRAS, 461, 3683, doi: [10.1093/mnras/stw1205](https://doi.org/10.1093/mnras/stw1205)
- Izotov, Y. I., Worseck, G., Schaerer, D., et al. 2018, MNRAS, 478, 4851, doi: [10.1093/mnras/sty1378](https://doi.org/10.1093/mnras/sty1378)
- Jaskot, A. E., & Oey, M. S. 2014, ApJL, 791, L19, doi: [10.1088/2041-8205/791/2/L19](https://doi.org/10.1088/2041-8205/791/2/L19)
- Jiang, T., Malhotra, S., Rhoads, J. E., & Yang, H. 2019, ApJ, 872, 145, doi: [10.3847/1538-4357/aeee8a](https://doi.org/10.3847/1538-4357/aeee8a)
- Kauffmann, G., Heckman, T. M., Tremonti, C., et al. 2003, MNRAS, 346, 1055, doi: [10.1111/j.1365-2966.2003.07154.x](https://doi.org/10.1111/j.1365-2966.2003.07154.x)
- Kennicutt, Jr., R. C. 1998, ARA&A, 36, 189, doi: [10.1146/annurev.astro.36.1.189](https://doi.org/10.1146/annurev.astro.36.1.189)

Table 2. Properties of the 26 spectroscopically observed DES-GPs

GP ID	R.A.	Decl.	m_r	z_{spec}	$\log(M_*)$	$\log(\text{SFR})_{\text{SED}}$	$\log(\text{SFR})_{\text{H}\alpha}$	$12 + \log(\text{O}/\text{H})$
	[deg]	[deg]	[mag]		[M_\odot]	[$M_\odot \text{ yr}^{-1}$]	[$M_\odot \text{ yr}^{-1}$]	
(1)	(2)	(3)	(4)	(5)	(6)	(7)	(8)	(9)
GP000207–424024	0.52965	-42.67360	20.02	0.3972	9.25	1.35	1.52	8.21
GP000957+024146	2.48999	2.69620	19.94	0.3379	9.29	0.89	1.44	8.25
GP001034–484901	2.64247	-48.81700	19.68	0.3059	9.08	0.24	1.73	8.02
GP005423+033009	13.59997	3.50259	19.95	0.3590	9.44	0.81	1.27	8.29
GP012256–154025	20.73453	-15.67363	20.24	0.3160	9.06	0.72	1.43	8.14
GP022429–105748	36.12384	-10.96339	20.33	0.3154	9.36	1.63	1.45	8.10
GP024352+035504	40.96804	3.91804	20.37	0.3890	8.92	0.79	1.42	8.19
GP031823–412811	49.59743	-41.46982	20.12	0.3972	9.06	0.83	1.71	8.19
GP033528–562307	53.86939	-56.38553	20.38	0.3825	8.76	0.83	0.97	8.07
GP035844–272134	59.68538	-27.35972	19.73	0.3169	9.18	0.83	1.70	8.03
GP042045–600735	65.18795	-60.12648	20.19	0.3651	9.00	0.73	1.48	8.13
GP043224–383800	68.10077	-38.63352	19.95	0.3200	9.48	0.57	1.39	8.17
GP051716–265543	79.31926	-26.92878	20.23	0.3505	8.60	0.89	1.60	8.05
GP052936–362507	82.40206	-36.41871	20.12	0.3052	8.89	1.03	1.39	8.00
GP054214–354139	85.56175	-35.69434	20.29	0.3605	9.11	1.16	1.35	8.23
GP204045–413555	310.19069	-41.59872	20.39	0.4030	8.86	1.29	1.22	7.98
GP204359–540359	310.99793	-54.06650	20.14	0.4126	9.29	1.35	1.75	8.19
GP210903–444951	317.26582	-44.83095	20.43	0.3105	8.77	0.93	0.91	8.07
GP211040–504353	317.66717	-50.73162	20.34	0.3126	8.64	1.24	1.24	8.08
GP211619–463914	319.08056	-46.65399	20.38	0.3951	8.71	1.03	0.70	8.22
GP212733–424114	321.88912	-42.68739	20.44	0.4060	9.15	1.36	1.05	8.15
GP213914–495028	324.81073	-49.84135	20.20	0.3947	8.81	0.87	1.15	8.23
GP215810–615644	329.54441	-61.94577	20.40	0.3364	9.20	0.66	1.14	8.18
GP232739–454554	351.91373	-45.76512	20.18	0.3965	9.05	1.36	2.62	8.13
GP234638–011839	356.65857	-1.31104	19.71	0.3671	9.49	0.87	1.38	8.15
GP234647+022744	356.69968	2.46240	20.01	0.3343	9.04	1.18	1.01	8.15

NOTE—(5): spectroscopic redshifts measured using the redshifted $[\text{OIII}]_{5007}$ emission lines; (6): stellar mass from the SED fitting (Section 3.1); (7): SFR from the SED fitting (Section 3.1); (8): SFR from the extinction-corrected $\text{H}\alpha$ line flux (using the method from Kennicutt 1998); (9): oxygen abundance based on the $N2$ method (Section 4.6)

- Kewley, L. J., Dopita, M. A., Sutherland, R. S., Heisler, C. A., & Trevena, J. 2001, *ApJ*, 556, 121, doi: [10.1086/321545](https://doi.org/10.1086/321545)
- Kewley, L. J., Groves, B., Kauffmann, G., & Heckman, T. 2006, *MNRAS*, 372, 961, doi: [10.1111/j.1365-2966.2006.10859.x](https://doi.org/10.1111/j.1365-2966.2006.10859.x)
- Kim, K., Malhotra, S., Rhoads, J. E., Butler, N. R., & Yang, H. 2020, *ApJ*, 893, 134, doi: [10.3847/1538-4357/ab7895](https://doi.org/10.3847/1538-4357/ab7895)
- Kim, K. J., Malhotra, S., Rhoads, J. E., & Yang, H. 2021, *ApJ*, 914, 2, doi: [10.3847/1538-4357/abf833](https://doi.org/10.3847/1538-4357/abf833)
- Labrie, K., Simpson, C., Cardenas, R., et al. 2023, *Research Notes of the American Astronomical Society*, 7, 214, doi: [10.3847/2515-5172/ad0044](https://doi.org/10.3847/2515-5172/ad0044)
- Li, L., Zhang, J., Peter, H., et al. 2018, *ApJ*, 868, L33, doi: [10.3847/2041-8213/aaf167](https://doi.org/10.3847/2041-8213/aaf167)
- Liu, S., Luo, A. L., Yang, H., et al. 2022, *ApJ*, 927, 57, doi: [10.3847/1538-4357/ac4bd9](https://doi.org/10.3847/1538-4357/ac4bd9)
- Lumbreras-Calle, A., López-Sanjuan, C., Sobral, D., et al. 2022, *A&A*, 668, A60, doi: [10.1051/0004-6361/202142898](https://doi.org/10.1051/0004-6361/202142898)
- Luo, A. L., Zhao, Y.-H., Zhao, G., et al. 2015, *Research in Astronomy and Astrophysics*, 15, 1095, doi: [10.1088/1674-4527/15/8/002](https://doi.org/10.1088/1674-4527/15/8/002)
- Marocco, F., Eisenhardt, P. R. M., Fowler, J. W., et al. 2021, *ApJS*, 253, 8, doi: [10.3847/1538-4365/abd805](https://doi.org/10.3847/1538-4365/abd805)
- McKinney, J. H., Jaskot, A. E., Oey, M. S., et al. 2019, *ApJ*, 874, 52, doi: [10.3847/1538-4357/ab08eb](https://doi.org/10.3847/1538-4357/ab08eb)
- McMahon, R. G., Banerji, M., Gonzalez, E., et al. 2021, *VizieR Online Data Catalog: The VISTA Hemisphere Survey (VHS) catalog DR5 (McMahon+, 2020), VizieR On-line Data Catalog: II/367. Originally published in: 2013Msngr.154...35M*
- Pettini, M., & Pagel, B. E. J. 2004, *MNRAS*, 348, L59, doi: [10.1111/j.1365-2966.2004.07591.x](https://doi.org/10.1111/j.1365-2966.2004.07591.x)
- Planck Collaboration, Aghanim, N., Akrami, Y., et al. 2020, *A&A*, 641, A6, doi: [10.1051/0004-6361/201833910](https://doi.org/10.1051/0004-6361/201833910)

Table 3. Emission line flux measurements in 26 DES-GPs

GP ID	H α	H β	[OII] _{3727,3729}	[OIII] ₄₉₅₉	[OIII] ₅₀₀₇	[NII] ₆₅₈₄	[SII] ₆₇₁₇	[SII] ₆₇₃₁
GP000207–424024	52.40 ± 0.19	15.87 ± 0.20	24.59 ± 0.90	21.19 ± 0.22	70.81 ± 0.35	3.20 ± 0.08	1.09 ± 0.09	1.72 ± 0.14
GP000957+024146	44.06 ± 0.20	11.21 ± 0.30	11.30 ± 1.50	17.36 ± 0.31	50.19 ± 0.48	3.19 ± 0.11	2.81 ± 0.12	2.32 ± 0.12
GP001034–484901	68.54 ± 0.26	14.06 ± 0.37	16.10 ± 1.90	28.02 ± 0.45	67.35 ± 0.48	1.97 ± 0.12	3.72 ± 0.18	2.20 ± 0.13
GP005423+033009	23.60 ± 0.25	5.79 ± 0.36	7.60 ± 1.80	6.87 ± 0.38	24.22 ± 0.37	2.00 ± 0.15	1.78 ± 0.12	1.23 ± 0.15
GP012256–154025	63.30 ± 0.36	18.10 ± 0.38	32.70 ± 3.00	34.50 ± 0.41	99.30 ± 0.50	2.95 ± 0.19	4.98 ± 0.20	3.15 ± 0.16
GP022429–105748	57.80 ± 0.31	15.40 ± 0.29	...	32.50 ± 0.32	103.00 ± 0.47	2.32 ± 0.16	3.37 ± 0.19	2.55 ± 0.11
GP024352+035504	34.80 ± 0.17	9.54 ± 0.20	16.40 ± 1.30	16.10 ± 0.21	55.10 ± 0.28	1.95 ± 0.11	1.99 ± 0.16	1.55 ± 0.09
GP031823–412811	65.90 ± 0.23	18.20 ± 0.26	31.60 ± 1.30	30.40 ± 0.28	95.70 ± 0.37	3.77 ± 0.11	2.71 ± 0.20	3.09 ± 0.20
GP033528–562307	16.00 ± 0.12	4.85 ± 0.23	7.60 ± 1.30	9.32 ± 0.15	27.90 ± 0.23	0.56 ± 0.07	0.95 ± 0.07	0.71 ± 0.13
GP035844–272134	130.00 ± 0.37	38.80 ± 0.36	46.80 ± 2.40	78.40 ± 0.46	237.00 ± 0.73	3.92 ± 0.13	5.89 ± 0.12	4.41 ± 0.13
GP042045–600735	49.00 ± 0.29	13.80 ± 0.29	18.30 ± 2.20	27.50 ± 0.31	81.20 ± 0.42	2.17 ± 0.17	2.32 ± 0.11	1.97 ± 0.11
GP043224–383800	45.30 ± 0.30	11.70 ± 0.35	19.00 ± 2.70	20.60 ± 0.37	60.90 ± 0.41	2.41 ± 0.13	3.97 ± 0.16	3.08 ± 0.22
GP051716–265543	68.10 ± 0.28	18.70 ± 0.31	21.60 ± 2.10	37.70 ± 0.45	114.00 ± 0.47	2.22 ± 0.22	2.42 ± 0.12	1.82 ± 0.11
GP052936–362507	65.50 ± 0.24	19.10 ± 0.35	23.80 ± 2.40	37.50 ± 0.36	112.00 ± 0.49	1.76 ± 0.11	3.64 ± 0.22	2.55 ± 0.15
GP054214–354139	35.10 ± 0.24	9.53 ± 0.26	20.80 ± 1.90	16.00 ± 0.27	49.20 ± 0.34	2.33 ± 0.18	2.93 ± 0.13	2.08 ± 0.12
GP204045–413555	26.19 ± 0.09	8.07 ± 0.12	...	15.71 ± 0.14	46.17 ± 0.17	0.65 ± 0.04	0.49 ± 0.09	0.31 ± 0.11
GP204359–540359	41.20 ± 0.16	9.11 ± 0.17	17.10 ± 0.93	20.36 ± 0.18	61.66 ± 0.24	2.34 ± 0.11	1.86 ± 0.10	1.45 ± 0.13
GP210903–444951	20.90 ± 0.18	6.07 ± 0.36	...	11.18 ± 0.31	34.79 ± 0.35	0.72 ± 0.16	0.98 ± 0.11	0.69 ± 0.10
GP211040–504353	40.48 ± 0.20	11.32 ± 0.27	9.60 ± 1.30	25.18 ± 0.28	73.95 ± 0.36	1.49 ± 0.16	1.58 ± 0.09	1.37 ± 0.13
GP211619–463914	12.25 ± 0.18	4.56 ± 0.23	5.18 ± 0.66	9.35 ± 0.22	31.19 ± 0.29	0.77 ± 0.10	0.57 ± 0.10	0.47 ± 0.11
GP212733–424114	16.98 ± 0.10	5.16 ± 0.16	5.26 ± 0.51	8.87 ± 0.16	26.39 ± 0.18	0.84 ± 0.09	0.90 ± 0.11	0.93 ± 0.09
GP213914–495028	23.10 ± 0.18	7.11 ± 0.21	7.76 ± 0.86	13.81 ± 0.21	40.78 ± 0.30	1.52 ± 0.11	0.94 ± 0.11	0.50 ± 0.12
GP215810–615644	19.61 ± 0.18	4.72 ± 0.20	...	8.58 ± 0.21	26.02 ± 0.32	1.09 ± 0.09	1.59 ± 0.08	1.13 ± 0.08
GP232739–454554	17.23 ± 0.14	0.94 ± 0.15	...	2.18 ± 0.17	8.56 ± 0.22	0.78 ± 0.08	...	0.86 ± 0.10
GP234638–011839	43.70 ± 0.26	13.00 ± 0.41	24.00 ± 1.90	22.27 ± 0.37	68.20 ± 0.47	2.12 ± 0.20	2.36 ± 0.14	1.85 ± 0.12
GP234647+022744	28.42 ± 0.20	9.31 ± 0.27	...	16.98 ± 0.26	46.04 ± 0.39	1.39 ± 0.15	1.40 ± 0.13	0.94 ± 0.09

NOTE—Line fluxes are in units of 10^{-16} erg s $^{-1}$ cm $^{-2}$.

Rhoads, J. E., Wold, I. G. B., Harish, S., et al. 2023, ApJL, 942, L14, doi: [10.3847/2041-8213/acaaf](https://doi.org/10.3847/2041-8213/acaaf)

Schaerer, D., Marques-Chaves, R., Barrufet, L., et al. 2022, A&A, 665, L4, doi: [10.1051/0004-6361/202244556](https://doi.org/10.1051/0004-6361/202244556)

Sevilla-Noarbe, I., Hoyle, B., Marchã, M. J., et al. 2018, MNRAS, 481, 5451, doi: [10.1093/mnras/sty2579](https://doi.org/10.1093/mnras/sty2579)

Speagle, J. S., Steinhardt, C. L., Capak, P. L., & Silverman, J. D. 2014, ApJS, 214, 15, doi: [10.1088/0067-0049/214/2/15](https://doi.org/10.1088/0067-0049/214/2/15)

Tang, M., Stark, D. P., Chevallard, J., & Charlot, S. 2019, MNRAS, 489, 2572, doi: [10.1093/mnras/stz2236](https://doi.org/10.1093/mnras/stz2236)

Tran, K.-V. H., Forrest, B., Alcorn, L. Y., et al. 2020, ApJ, 898, 45, doi: [10.3847/1538-4357/ab8c8a](https://doi.org/10.3847/1538-4357/ab8c8a)

Tremonti, C. A., Heckman, T. M., Kauffmann, G., et al. 2004, ApJ, 613, 898, doi: [10.1086/423264](https://doi.org/10.1086/423264)

Yang, H., Malhotra, S., Gronke, M., et al. 2016, ApJ, 820, 130, doi: [10.3847/0004-637X/820/2/130](https://doi.org/10.3847/0004-637X/820/2/130)

Yang, H., Malhotra, S., Rhoads, J. E., et al. 2017a, ApJ, 838, 4, doi: [10.3847/1538-4357/aa6337](https://doi.org/10.3847/1538-4357/aa6337)

Yang, H., Malhotra, S., Rhoads, J. E., & Wang, J. 2017b, ApJ, 847, 38, doi: [10.3847/1538-4357/aa8809](https://doi.org/10.3847/1538-4357/aa8809)

York, D. G., Adelman, J., Anderson, John E., J., et al. 2000, AJ, 120, 1579, doi: [10.1086/301513](https://doi.org/10.1086/301513)

Table 4. Observed equivalent width measurements in 26 DES-GPs

GP ID	H α	H β	[OII] _{3727,3729}	[OIII] ₄₉₅₉	[OIII] ₅₀₀₇	[NII] ₆₅₈₄	[SII] ₆₇₁₇	[SII] ₆₇₃₁
GP000207–424024	260 \pm 7	91 \pm 6	67 \pm 13	120 \pm 7	421 \pm 15	14 \pm 2	14 \pm 4	22 \pm 9
GP000957+024146	442 \pm 11	63 \pm 8	27 \pm 15	91 \pm 8	223 \pm 11	31 \pm 5	33 \pm 7	35 \pm 8
GP001034–484901	422 \pm 9	49 \pm 5	33 \pm 15	112 \pm 9	267 \pm 10	12 \pm 3	36 \pm 8	23 \pm 6
GP005423+033009	199 \pm 12	23 \pm 7	8 \pm 8	24 \pm 6	89 \pm 7	19 \pm 6	15 \pm 5	11 \pm 6
GP012256–154025	452 \pm 14	61 \pm 6	28 \pm 10	120 \pm 7	323 \pm 8	20 \pm 5	56 \pm 9	22 \pm 5
GP022429–105748	671 \pm 20	96 \pm 8	...	175 \pm 7	543 \pm 12	29 \pm 9	43 \pm 11	33 \pm 6
GP024352+035504	418 \pm 12	58 \pm 6	38 \pm 13	98 \pm 7	313 \pm 9	24 \pm 6	27 \pm 9	21 \pm 5
GP031823–412811	598 \pm 13	78 \pm 5	47 \pm 9	131 \pm 6	372 \pm 8	32 \pm 4	22 \pm 7	26 \pm 7
GP033528–562307	357 \pm 15	50 \pm 10	21 \pm 14	74 \pm 5	238 \pm 10	13 \pm 7	23 \pm 8	18 \pm 14
GP035844–272134	586 \pm 9	120 \pm 5	50 \pm 12	248 \pm 8	755 \pm 13	20 \pm 2	39 \pm 3	30 \pm 3
GP042045–600735	457 \pm 16	73 \pm 7	19 \pm 10	121 \pm 7	372 \pm 10	22 \pm 8	21 \pm 4	21 \pm 5
GP043224–383800	390 \pm 13	52 \pm 7	17 \pm 10	80 \pm 7	233 \pm 8	23 \pm 5	40 \pm 7	31 \pm 12
GP051716–265543	796 \pm 21	87 \pm 7	26 \pm 12	141 \pm 8	470 \pm 11	25 \pm 11	25 \pm 6	20 \pm 5
GP052936–362507	435 \pm 9	75 \pm 7	22 \pm 8	144 \pm 7	391 \pm 10	12 \pm 3	30 \pm 8	21 \pm 5
GP054214–354139	371 \pm 13	50 \pm 6	22 \pm 8	76 \pm 6	233 \pm 8	26 \pm 7	32 \pm 7	23 \pm 5
GP204045–413555	455 \pm 9	76 \pm 5	...	159 \pm 7	467 \pm 9	11 \pm 2	22 \pm 12	12 \pm 16
GP204359–540359	414 \pm 10	75 \pm 7	41 \pm 11	174 \pm 8	520 \pm 14	30 \pm 8	24 \pm 6	18 \pm 7
GP210903–444951	246 \pm 11	33 \pm 9	...	59 \pm 7	193 \pm 9	7 \pm 6	10 \pm 4	9 \pm 5
GP211040–504353	405 \pm 11	63 \pm 6	13 \pm 6	155 \pm 7	332 \pm 7	17 \pm 7	27 \pm 6	18 \pm 6
GP211619–463914	127 \pm 26	46 \pm 10	22 \pm 10	111 \pm 11	319 \pm 12	52 \pm 32	16 \pm 9	14 \pm 11
GP212733–424114	496 \pm 14	66 \pm 9	27 \pm 11	106 \pm 8	325 \pm 10	24 \pm 11	29 \pm 12	29 \pm 10
GP213914–495028	492 \pm 24	59 \pm 8	22 \pm 11	132 \pm 9	308 \pm 12	33 \pm 11	27 \pm 12	9 \pm 6
GP215810–615644	446 \pm 25	38 \pm 7	...	72 \pm 8	219 \pm 13	26 \pm 10	70 \pm 18	106 \pm 29
GP232739–454554	334 \pm 16	8 \pm 5	...	22 \pm 7	95 \pm 12	16 \pm 7	...	19 \pm 9
GP234638–011839	298 \pm 11	43 \pm 8	37 \pm 13	66 \pm 6	227 \pm 10	18 \pm 7	19 \pm 6	15 \pm 4
GP234647+022744	471 \pm 19	70 \pm 10	...	127 \pm 10	356 \pm 16	26 \pm 14	31 \pm 13	21 \pm 10

NOTE—Equivalent widths are in units of \AA .